

# AN EXPLICIT DIVERGENCE-FREE DG METHOD FOR INCOMPRESSIBLE FLOW

GUOSHENG FU

**ABSTRACT.** We present an explicit divergence-free DG method for incompressible flow based on velocity formulation only. An  $H(\text{div})$ -conforming, and globally divergence-free finite element space is used for the velocity field, and the pressure field is eliminated from the equations by design. The resulting ODE system can be discretized using any explicit time stepping methods. We use the third order strong-stability preserving Runge-Kutta method in our numerical experiments. Our spatial discretization produces the *identical* velocity field as the divergence-conforming DG method of Cockburn et al. [8] based on a velocity-pressure formulation, when the same DG operators are used for the convective and viscous parts.

Due to the global nature of the divergence-free constraint and its interplay with the boundary conditions, it is very hard to construct local bases for our finite element space. Here we present a key result on the efficient implementation of the scheme by identifying the equivalence of the mass matrix inversion of the globally divergence-free finite element space to a standard (hybrid-)mixed Poisson solver. Hence, in each time step, a (hybrid-)mixed Poisson solver is used, which reflects the global nature of the incompressibility condition. In the actual implementation of this fully discrete scheme, the pressure field is also computed (via the hybrid-mixed Poisson solver). Hence, the scheme can be interpreted as a velocity-pressure formulation that treat the incompressibility constraint and pressure forces implicitly, but the viscous and convective part explicitly. Since we treat viscosity explicitly for the Navier-Stokes equation, our method shall be best suited for unsteady high-Reynolds number flows so that the CFL constraint is not too restrictive.

## 1. INTRODUCTION

It is highly desirable to have a velocity field that is point-wisely divergence-free (exactly mass conservation) for incompressible flows; see the recent review article [17].

We propose a new explicit, high-order, divergence-free DG scheme for the unsteady incompressible Euler and Navier-Stokes equation based on a *solely* velocity formulation. The pressure field and incompressibility constraint are eliminated from the equation by design. Our semi-discrete scheme produce exactly the same velocity field as the divergence-conforming DG method of Cockburn et al. [8]. Hence, our scheme enjoys features such as global and local conservation properties, high-order accuracy, energy-stability, and pressure-robustness [8, 16].

The resulting semi-discrete scheme is an ODE system for velocity only, as opposite to the differential-algebraic equations (DAE) in [8] where the pressure field and incompressibility-constraint enter into the equations directly. As a consequence, we can apply any explicit time-stepping techniques to solve the ODE system. Our

---

1991 *Mathematics Subject Classification.* 65N30, 65N12, 76S05, 76D07.

explicit fully-discrete scheme is also equivalence to the velocity-pressure formulation [8] coupled with corresponding explicit treatments for the convective and viscous parts, and implicit treatments for the pressure forces and divergence-free constraint. Such temporal treatment has already been briefly discussed in [19, Section 3.2.1].

Within each time step, the mass matrix for the divergence-free finite element space shall be inverted. Due to the non-locality of the divergence-free constraint in the finite element space and its interplay with the boundary conditions, it is very hard, if possible, to construct the local bases. Here we consider alternative formulations for the efficient implementation of the fully-discrete scheme. In particular, we either relax the divergence-free condition or the divergence-conformity condition in the finite elements via proper Lagrange multipliers, which yields a mixed Poisson solver or a hybrid-mixed Poisson solver in each time stage. The hybrid-mixed formulation is used in our numerical simulations.

We treat the viscosity term explicitly to avoid a Stokes solver. Hence, our scheme shall be applied to unsteady high-Reynolds number, unresolved flows so that the CFL constraint is not too restrictive. Roughly speaking, when both convective and viscous terms are treated explicitly as in our scheme, the following time stepping restriction for stability is to be expected

$$\Delta t \leq \min \left\{ c_C \frac{h}{k^2} \frac{1}{v_{\max}}, c_B \frac{h^2}{k^4} \frac{1}{\nu} \right\},$$

where  $\Delta t$  is the time step size,  $h$  is the mesh size,  $k$  is the polynomial degree in the finite elements,  $v_{\max}$  is the maximal velocity magnitude,  $\nu$  is the viscosity coefficient, and  $c_B, c_C > 0$  are the CFL stability constants for the convective and viscous parts, respectively. If we denote the mesh Reynolds number  $\text{Re}_h$  as

$$\text{Re}_h := \frac{v_{\max} h}{\nu k^2}, \quad (1)$$

then the above time stepping restriction becomes

$$\Delta t \leq \min \{c_C, c_B \text{Re}_h\} \frac{h}{k^2} \frac{1}{v_{\max}}. \quad (2)$$

Hence, as long as the mesh Reynolds number  $\text{Re}_h \gg 1$  (unresolved flow), or  $c_C \approx c_B \text{Re}_h$  (slightly resolved flow), the explicit treatment of viscous term does not pose extra severe time-stepping restrictions besides the CFL constraint from the explicit convection treatment.

On the other hand, when  $\text{Re}_h \ll 1$ , i.e., when the flow is highly resolved, explicit treatment of the viscous term would not be efficient anymore. In this case, we suggest to treat the viscous term implicitly with a divergence-conforming hybridizable DG (HDG) method [19, 20]. Therein, various *stiffly accurate* operator-splitting time integration approaches were discussed, including *additive* decomposition methods like IMplicit-EXplicit(IMEX) schemes [4, 7, 18], *product* decomposition methods like the operator-integration-factor splittings [22], and an operator-splitting modification of the fractional step method [14].

Comparing with other schemes that treat viscosity explicitly, the computational cost of our scheme is comparable to the DG scheme based on a vorticity-stream function formulation [21] in two dimensions, and is a lot cheaper than the vorticity-vector potential formulation [10] in three dimensions. A significant computational

saving per time step (one hybrid-mixed Poisson solver/step) is achieved comparing with methods that treat viscosity term implicitly, e.g. the IMEX divergence-conforming HDG scheme [20] (one Stokes solver/step) or the projection methods [15] ( $d + 1$  Poisson solver/step with  $d$  the space dimension). Finally, we shall mention that boundary condition is easy to impose for our velocity-based formulation (and for various mixed methods based on velocity-pressure formulations [17]), while that consists one of the major bottlenecks for vorticity-based methods [9] or projection methods [15].

The rest of the paper is organized as follows. In Section 2, the explicit divergence-free DG scheme is introduced for the incompressible Euler equation, along with a key result on transforming the mass matrix inversion to a hybrid-mixed Poisson solver. In Section 3, the scheme is extended to the incompressible Navier-Stokes equations. Extensive numerical results in two dimensions are presented in Section 4. Finally we conclude in Section 5.

## 2. EULER EQUATIONS

We consider the following incompressible Euler equations:

$$\partial_t \mathbf{u} + (\mathbf{u} \cdot \nabla) \mathbf{u} + \nabla p = \mathbf{f}, \quad \text{in } \Omega, \quad (3a)$$

$$\nabla \cdot \mathbf{u} = 0, \quad \text{in } \Omega, \quad (3b)$$

$$\mathbf{u} \cdot \mathbf{n} = g, \quad \text{on } \partial\Omega, \quad (3c)$$

with initial condition

$$\mathbf{u}(x, 0) = \mathbf{u}_0(x) \quad \forall x \in \Omega,$$

where  $\mathbf{u}$  is the velocity and  $p$  is the pressure,  $\Omega \subset \mathbb{R}^d$  ( $d=2,3$ ) is a polygonal/polyhedral domain, and  $\mathbf{n}$  is the outward normal direction on the domain boundary  $\partial\Omega$ . The initial velocity  $\mathbf{u}_0(x)$  is assumed to be divergence-free. For simplicity, we assume no source/sink and no-flow boundary conditions,  $\mathbf{f} = 0$  and  $g = 0$ . The inflow/outflow boundary conditions will be discussed at the end of this section.

**2.1. Preliminaries.** Let  $\mathcal{T}_h$  be a conforming simplicial triangulation of  $\Omega$ . For any element  $T \in \mathcal{T}_h$ , we denote by  $h_T$  its diameter and we denote by  $h$  the maximum diameter over all mesh elements. Denote by  $\mathcal{F}_h$  the set of facets of  $\mathcal{T}_h$ , and by  $\mathcal{F}_h^i = \mathcal{F}_h \setminus \partial\Omega$  the set of interior facets.

We denote the following set of finite element spaces:

$$\mathbf{V}_{h,\text{dg}}^k := \prod_{T \in \mathcal{T}_h} [\mathbb{P}^k(T)]^d, \quad (4a)$$

$$\mathbf{V}_{h,\text{dg}}^{k,m} := \{\mathbf{v} \in \mathbf{V}_{h,\text{dg}}^k, \nabla \cdot \mathbf{v}|_T \in \mathbb{P}^m(T) \quad \forall T \in \mathcal{T}_h\}, \quad (4b)$$

$$\mathbf{V}_h^k := \{\mathbf{v} \in \mathbf{V}_{h,\text{dg}}^k, \llbracket \mathbf{v} \cdot \mathbf{n} \rrbracket_F = 0 \quad \forall F \in \mathcal{F}_h\} \subset H_0(\text{div}, \Omega), \quad (4c)$$

$$\mathbf{V}_h^{k,m} := \{\mathbf{v} \in \mathbf{V}_h^k, \nabla \cdot \mathbf{v} \in \mathbb{P}^m(T) \quad \forall T \in \mathcal{T}_h\}, \quad (4d)$$

$$\mathbf{Q}_h^m := \left( \prod_{T \in \mathcal{T}_h} \mathbb{P}^m(T) \right) \cap L_0^2(\Omega), \quad (4e)$$

$$\mathbf{M}_h^k := \prod_{F \in \mathcal{F}_h} \mathbb{P}^k(F), \quad (4f)$$

where the polynomial degree  $k \geq 1$  and  $-1 \leq m \leq k-1$ , and  $\llbracket \cdot \rrbracket$  is the usual jump operator and  $\mathbb{P}^r$  the space of polynomials up to degree  $r$  with the convention that

$\mathbb{P}^{-1} = \{0\}$ . Note that functions in  $M_h^k$  are defined only on the mesh skeleton  $\mathcal{F}_h$ , which will be used in the hybrid-mixed Poisson solver.

Finally, we introduce the jump and average notation. Let  $\phi_h$  be any function in  $\mathbf{V}_{h,\text{dg}}^k$ . On each facet  $F \in \mathcal{F}_h^i$  shared by two elements  $K^-$  and  $K^+$ , we denote  $(\phi_h)^\pm|_F = (\phi_h)|_{K^\pm}$ , and use

$$[\![\phi_h]\!]_F = \phi_h^+ \cdot \mathbf{n}^+ + \phi_h^- \cdot \mathbf{n}^-, \quad \{\!\!\{\phi_h\}\!\!\}_F = \frac{1}{2}(\phi_h^+ + \phi_h^-) \quad (5)$$

to denote the jump and the average of  $\phi_h \in V_h^k$  on the facet  $F$ .

**2.2. Spatial discretization.** The divergence-free space  $\mathbf{V}_h^{k,-1}$  shall be used in our DG formulation. With this space in use, the divergence-free constraint (3b) is pointwisely satisfied by design, and the pressure do not enter into the weak formulation of the scheme. The semi-discrete scheme reads as follows: find  $\mathbf{u}_h(t) \in \mathbf{V}_h^{k,-1}$  such that

$$(\partial_t \mathbf{u}_h, \mathbf{v}_h)_{\mathcal{T}_h} + \mathcal{C}_h(\mathbf{u}_h; \mathbf{u}_h, \mathbf{v}_h) = 0, \quad \forall \mathbf{v}_h \in \mathbf{V}_h^{k,-1}. \quad (6)$$

where  $(\cdot, \cdot)_{\mathcal{T}_h}$  denotes the standard  $L^2$ -inner product, and the *upwinding* trilinear form

$$\mathcal{C}_h(\mathbf{u}_h; \mathbf{u}_h, \mathbf{v}_h) := \sum_{T \in \mathcal{T}_h} \int_T -(\mathbf{u}_h \otimes \mathbf{u}_h) : \nabla \mathbf{v}_h \, dx + \int_{\partial T} (\mathbf{u}_h \cdot \mathbf{n})(\mathbf{u}_h^- \cdot \mathbf{v}_h) \, ds \quad (7)$$

where the upwinding numerical flux  $\mathbf{u}_h^-|_F = \mathbf{u}_h|_{K^-}$  with  $K^-$  being the element such that its outward normal direction  $\mathbf{n}^-$  on the facet  $F$  satisfies  $\mathbf{u}_h^- \cdot \mathbf{n}^- \geq 0$  (outflow boundary).

Since

$$\mathcal{C}_h(\mathbf{u}_h; \mathbf{u}_h, \mathbf{u}_h) = \sum_{F \in \mathcal{F}_h^i} \int_F |\mathbf{u}_h \cdot \mathbf{n}| ([\![\mathbf{u}_h]\!] \cdot [\![\mathbf{u}_h]\!]) \, ds \geq 0,$$

the scheme (6) is energy-stable in the sense that

$$\partial_t \|\mathbf{u}_h^2(t)\|_{\mathcal{T}_h} \leq 0,$$

where  $\|\cdot\|_{\mathcal{T}_h}$  denotes the  $L^2$ -norm on  $\mathcal{T}_h$ .

**2.3. Temporal discretization.** The semi-discrete scheme (6) can be written as

$$\mathcal{M}(\partial_t \mathbf{u}_h) = \mathcal{L}(\mathbf{u}_h),$$

where  $\mathcal{M}$  is the mass matrix for the space  $\mathbf{V}_h^{k,-1}$ , and  $\mathcal{L}(\mathbf{u}_h)$  the spatial discretization operator. Any explicit time stepping techniques can be applied to the scheme (6). We use the following three-stage, third-order strong-stability preserving Runge-Kutta method (TVD-RK3) [29] in our numerical experiments:

$$\begin{aligned} \mathcal{M}\mathbf{u}_h^{(1)} &= \mathcal{M}\mathbf{u}_h^n + \Delta t^n \mathcal{L}(\mathbf{u}_h^n), \\ \mathcal{M}\mathbf{u}_h^{(2)} &= \frac{3}{4}\mathcal{M}\mathbf{u}_h^n + \frac{1}{4} \left[ \mathcal{M}\mathbf{u}_h^{(1)} + \Delta t^n \mathcal{L}(\mathbf{u}_h^{(1)}) \right], \\ \mathcal{M}\mathbf{u}_h^{n+1} &= \frac{1}{3}\mathcal{M}\mathbf{u}_h^n + \frac{2}{3} \left[ \mathcal{M}\mathbf{u}_h^{(2)} + \Delta t^n \mathcal{L}(\mathbf{u}_h^{(2)}) \right], \end{aligned} \quad (8)$$

where  $\mathbf{u}_h^n$  is the given velocity at time level  $t^n$  and  $\mathbf{u}_h^{n+1}$  is the computed velocity at time level  $t^{n+1} = t^n + \Delta t^n$ . In each time step, three mass matrix inversion is needed.

**Remark 1** (Implementation). *Despite the mathematical simplicity of the solely velocity based formulation (6) and the ease of using explicit time stepping methods of the resulting ODE system, to the best of our knowledge, the method was never directly implemented in the literature. The major obstacle is that the space  $\mathbf{V}_h^{k,-1}$  is not a standard finite element space whose basis functions can be easily defined, due to the built-in global divergence-free constraint and its interplay with the boundary conditions. By the finite element de Rham complex property [3], we have, in two dimensions,*

$$\mathbf{V}_h^{k,-1} = \nabla \times \left\{ \phi \in H^1(\Omega) : \phi|_T \in \mathbb{P}^{k+1}(T), \quad \forall T \in \mathcal{T}_h, \right. \\ \left. (\nabla \times \phi) \cdot \mathbf{n} = 0 \text{ on } \partial\Omega \right\},$$

where the two-dimension curl operator “ $\nabla \times$ ” is the rotated gradient, and, in three dimensions,

$$\mathbf{V}_h^{k,-1} = \nabla \times \left\{ \phi \in H(\text{curl}, \Omega) : \phi|_T \in [\mathbb{P}^{k+1}(T)]^3, \quad \forall T \in \mathcal{T}_h, \right. \\ \left. (\nabla \times \phi) \cdot \mathbf{n} = 0 \text{ on } \partial\Omega \right\}.$$

The difficulty of basis construction of this space in two dimensions lies in the treatment of the boundary condition for domain with more than one piece of connected boundary, which can be resolved by a weakly enforcement of boundary conditions. On the other hand, the difficulty of basis construction in three dimensions is more fundamental, which is due to the fact that the curl operator has a large kernel including all gradient fields.

In the next subsection, we introduce proper Lagrange multipliers to avoid the direct use of the divergence-free space  $\mathbf{V}_h^{k,-1}$ .

**2.4. Avoid bases construction for  $\mathbf{V}_h^{k,-1}$ .** In this subsection, we show an efficient implementation of the scheme coupled with forward Euler time stepping that avoid bases construction for the space  $\mathbf{V}_h^{k,-1}$ . The forward Euler scheme for (6) reads as follows: given the numerical solution at time  $t^n$ ,  $\mathbf{u}_h^n \in \mathbf{V}_h^{k,-1} \approx \mathbf{u}(t^n)$ , compute the solution at next time level  $\mathbf{u}_h^{n+1} \in \mathbf{V}_h^{k,-1} \approx \mathbf{u}(t^n + \Delta t^n)$  by the following set of equations:

$$(\mathbf{u}_h^{n+1}, \mathbf{v}_h)_{\mathcal{T}_h} = \underbrace{(\mathbf{u}_h^n, \mathbf{v}_h)_{\mathcal{T}_h} - \Delta t^n \mathcal{C}_h(\mathbf{u}_h^n; \mathbf{u}_h^n, \mathbf{v}_h)}_{:= \mathcal{F}^n(\mathbf{v}_h)}, \quad \forall \mathbf{v}_h \in \mathbf{V}_h^{k,-1}. \quad (9)$$

*Conversion to a mixed-Poisson solver (via a velocity-pressure formulation).* We introduce the following equivalent formulation of the scheme (9) that use a larger velocity space that is divergence-conforming, but not divergence-free: find  $(\mathbf{u}_{h,\text{mix}}^{n+1}, w_h^{n+1}) \in \mathbf{V}_h^k \times Q_h^{k-1}$  such that

$$(\mathbf{u}_{h,\text{mix}}^{n+1}, \mathbf{v}_h)_{\mathcal{T}_h} - (w_h^{n+1}, \nabla \cdot \mathbf{v}_h)_{\mathcal{T}_h} = \mathcal{F}^n(\mathbf{v}_h), \quad \forall \mathbf{v}_h \in \mathbf{V}_h^k, \quad (10a)$$

$$(\nabla \cdot \mathbf{u}_{h,\text{mix}}^{n+1}, z_h)_{\mathcal{T}_h} = 0 \quad \forall z_h \in Q_h^{k-1}. \quad (10b)$$

Since  $\mathbf{V}_h^k$  is the standard BDM space [6], the scheme (10) can be readily implemented. Notice that the scheme (10) is nothing but a mixed Poisson formulation (with a different right hand side vector), whose well-posedness is well-known.

The equivalence of schemes (9) and (10) is given below.

**Theorem 1.** *Let  $(\mathbf{u}_{h,\text{mix}}^{n+1}, w_h^{n+1}) \in \mathbf{V}_h^k \times Q_h^{k-1}$  be the unique solution to the equations (10). Then,  $\mathbf{u}_{h,\text{mix}}^{n+1} \in \mathbf{V}_h^{k,-1}$  solves the equations (9). Moreover, the quantity  $w_h^{n+1}/\Delta t^n$  is an approximation of the pressure field at time  $t^{n+1}$ .*

*Proof.* Since  $\nabla \cdot \mathbf{V}_h^k = Q_h^{k-1}$ , the equations (10b) implies that  $\nabla \cdot \mathbf{u}_{h,\text{mix}}^{n+1} = 0$ , hence  $\mathbf{u}_{h,\text{mix}}^{n+1} \in \mathbf{V}_h^{k,-1}$ . Taking  $\mathbf{v}_h \in \mathbf{V}_h^{k,-1}$  in equations (10a), we get

$$(\mathbf{u}_{h,\text{mix}}^{n+1}, \mathbf{v}_h)_{\mathcal{T}_h} = \mathcal{F}^n(\mathbf{v}_h).$$

Hence,  $\mathbf{u}_{h,\text{mix}}^{n+1} \in \mathbf{V}_h^{k,-1}$  is the solution to equations (9). The quantity  $w_h^{n+1}/\Delta t^n$  approximates the pressure variable is shown in Remark 2 below.  $\square$

**Remark 2** (Equivalence with the velocity-pressure formulation). *Recall that the semi-discrete velocity-pressure formulation [16] which use a divergence-conforming velocity space  $\mathbf{V}_h^k$  and the matching pressure space  $Q_h^{k-1}$  is to find  $(\mathbf{u}_h(t), p_h(t)) \in \mathbf{V}_h^k \times Q_h^{k-1}$  such that*

$$\begin{aligned} (\partial_t \mathbf{u}_h, \mathbf{v}_h)_{\mathcal{T}_h} - (p_h, \nabla \cdot \mathbf{v}_h)_{\mathcal{T}_h} + \mathcal{C}_h(\mathbf{u}_h; \mathbf{u}_h, \mathbf{v}_h) &= 0, \quad \forall \mathbf{v}_h \in \mathbf{V}_h^k, \\ (\nabla \cdot \mathbf{u}_h, q_h)_{\mathcal{T}_h} &= 0, \quad \forall q_h \in Q_h^{k-1}. \end{aligned}$$

*An first-order IMEX time discretization yields the fully-discrete scheme*

$$(\mathbf{u}_h^{n+1}, \mathbf{v}_h)_{\mathcal{T}_h} - (\Delta t^n p_h^{n+1}, \nabla \cdot \mathbf{v}_h)_{\mathcal{T}_h} = \mathcal{F}^n(\mathbf{v}_h), \quad \forall \mathbf{v}_h \in \mathbf{V}_h^k, \quad (11a)$$

$$(\nabla \cdot \mathbf{u}_h^{n+1}, q_h)_{\mathcal{T}_h} = 0, \quad \forall q_h \in Q_h^{k-1}, \quad (11b)$$

*which is easily seen to be identical to the scheme (10) introduced earlier by identifying  $w_h^{n+1}$  with  $\Delta t^n p_h^{n+1}$ . Hence, although we work with the velocity-only formulation (6) mathematically, in the numerical implementation, pressure is always simultaneously been calculated.*

*However, we point out that the formulation (10) is preferred over (11) in the actual numerical implementation due to the fact that the matrix resulting from the linear system never changes for variable time step size  $\Delta t^n$ , which is equivalent to a mixed Poisson solver.*

Although efficient solvers are available for the mixed-Poisson saddle point linear system (10), we prefer to use the celebrated hybridization technique [1] to convert it to a symmetric positive definition linear system, which is a lot easier to solve.

*Conversion to a hybrid-mixed Poisson solver.* The hybrid-mixed formulation is given below: find  $(\mathbf{u}_{h,\text{hyb}}^{n+1}, w_h^{n+1}, \lambda_h^{n+1}) \in \mathbf{V}_{h,\text{dg}}^k \times Q_h^{k-1} \times M_h^k$  such that

$$\begin{aligned} & (\mathbf{u}_{h,\text{mix}}^{n+1}, \mathbf{v}_h)_{\mathcal{T}_h} - (w_h^{n+1}, \nabla \cdot \mathbf{v}_h)_{\mathcal{T}_h} \\ & + \sum_{T \in \mathcal{T}_h} \int_{\partial T} \lambda_h^{n+1} (\mathbf{v}_h \cdot \mathbf{n}) \, ds = \mathcal{F}^n(\mathbf{v}_h), \quad \forall \mathbf{v}_h \in \mathbf{V}_{h,\text{dg}}^k, \end{aligned} \quad (12a)$$

$$(\nabla \cdot \mathbf{u}_{h,\text{mix}}^{n+1}, z_h)_{\mathcal{T}_h} = 0, \quad \forall z_h \in Q_h^{k-1}, \quad (12b)$$

$$\sum_{T \in \mathcal{T}_h} \int_{\partial T} \mu_h (\mathbf{u}_h \cdot \mathbf{n}) \, ds = 0 \quad \forall \mu_h \in M_h^k. \quad (12c)$$

After static condensation, the scheme (12) yields an SPD linear system for the Lagrange multiplier  $\lambda_h^{n+1}$ . The following equivalence result is now trivially true.

**Theorem 2.** *Let  $(\mathbf{u}_{h,\text{hyb}}^{n+1}, w_h^{n+1}, \lambda_h^{n+1}) \in \mathbf{V}_{h,\text{dg}}^k \times Q_h^{k-1} \times M_h^k$  be the unique solution to the equations (12). Then,  $\mathbf{u}_{h,\text{hyb}}^{n+1} \in \mathbf{V}_h^{k,-1}$  solves the equations (9). Moreover, the quantity  $w_h^{n+1}/\Delta t^n$  is an approximation of the pressure field at time  $t^{n+1}$  on the mesh  $\mathcal{T}_h$ , while the quantity  $\lambda_h^{n+1}/\Delta t^n$  is an approximation of the pressure field at time  $t^{n+1}$  on the mesh skeleton  $\mathcal{F}_h$ .*

**Remark 3** (More efficient implementation). *One can further improve the efficiency of this hybrid-mixed solver (12) by taking advantage of the divergence-free property of the velocity space. In particular, we can restrict the velocity space to be locally divergence-free  $\mathbf{V}_{h,\text{dg}}^{k,-1}$ , and remove the equations involving  $w_h^{n+1}$  and  $z_h$  in (12), which results in the following simplified scheme: find  $(\mathbf{u}_{h,\text{hyb}}^{n+1}, \lambda_h^{n+1}) \in \mathbf{V}_{h,\text{dg}}^{k,-1} \times M_h^k$  such that*

$$(\mathbf{u}_{h,\text{mix}}^{n+1}, \mathbf{v}_h)_{\mathcal{T}_h} - \sum_{T \in \mathcal{T}_h} \int_{\partial T} \lambda_h^{n+1} (\mathbf{v}_h \cdot \mathbf{n}) \, ds = \mathcal{F}^n(\mathbf{v}_h), \quad \forall \mathbf{v}_h \in \mathbf{V}_{h,\text{dg}}^{k,-1}, \quad (13a)$$

$$\sum_{T \in \mathcal{T}_h} \int_{\partial T} \mu_h (\mathbf{u}_h \cdot \mathbf{n}) \, ds = 0 \quad \forall \mu_h \in M_h^k. \quad (13b)$$

Note that local bases for the DG space  $\mathbf{V}_{h,\text{dg}}^{k,-1}$  can be easily constructed. We mention that such spatial discretization which use a locally divergence-free velocity space and a hybrid (facet) pressure space was already considered in [23].

Our numerical simulations are performed using the open-source finite-element software NGSolve [27], <https://ngsolve.org/>, in which we still use the formulation (12), but take the velocity space to be  $\mathbf{V}_{h,\text{dg}}^{k,0}$ , and the space for  $w_h^{n+1}$  to be piece-wise constants  $Q_h^0$ . The local bases for the space  $\mathbf{V}_{h,\text{dg}}^{k,0}$  for various element shapes can be found in [25].

**2.5. Inflow/outflow boundary conditions.** Finally, we briefly comment on the imposing of inflow/outflow boundary conditions. Suppose the Euler equation (3) is replaced with the following inflow/outflow/wall boundary conditions:

$$\mathbf{u} \cdot \mathbf{n} = u_{\text{in}} \quad \text{on } \Gamma_{\text{in}}, \quad \mathbf{u} \cdot \mathbf{n} = 0 \quad \text{on } \Gamma_{\text{wall}}, \quad p = 0 \quad \text{on } \Gamma_{\text{out}}, \quad (14)$$

with  $\partial\Omega = \Gamma_{in} \cup \Gamma_{wall} \cup \Gamma_{out}$ . Introducing the finite element spaces without/with boundary condition

$$\begin{aligned}\widetilde{\mathbf{V}}_h^{k,-1} &:= \left\{ \mathbf{v} \in \mathbf{V}_{h,dg}^{k,-1}, \llbracket \mathbf{v} \cdot \mathbf{n} \rrbracket_F = 0 \ \forall F \in \mathcal{F}_h^i \right\}, \\ \widetilde{\mathbf{V}}_{h,g}^{k,-1} &:= \left\{ \mathbf{v} \in \widetilde{\mathbf{V}}_h^{k,-1}, \ \mathbf{v} \cdot \mathbf{n} = \begin{cases} g & \text{on } \Gamma_{in}, \\ 0 & \text{on } \Gamma_{wall}. \end{cases} \right\}.\end{aligned}$$

Note that for any pressure field  $p \in H^1(\Omega)$  satisfying  $p = 0$  on  $\Gamma_{out}$ , the following identity holds,

$$\begin{aligned}\int_{\Omega} \nabla p \cdot \mathbf{v}_h dx &= - \int_{\Omega} p \nabla \cdot (\mathbf{v}_h) dx + \int_{\partial\Omega} p (\mathbf{v}_h \cdot \mathbf{n}) ds \\ &= \int_{\Gamma_{in} \cup \Gamma_{wall}} p (\mathbf{v}_h \cdot \mathbf{n}) ds, \quad \forall \mathbf{v}_h \in \widetilde{\mathbf{V}}_h^{k,-1}.\end{aligned}\tag{15}$$

In particular,  $\int_{\Omega} \nabla p \cdot \mathbf{v}_h dx = 0$  for all  $\mathbf{v}_h \in \widetilde{\mathbf{V}}_{h,0}^{k,-1}$ .

Then, the semi-discrete scheme for (3) with boundary condition (14) is to find  $\mathbf{u}_h(t) \in \widetilde{\mathbf{V}}_{h,u_{in}}^{k,-1}$  such that

$$(\partial_t \mathbf{u}_h, \mathbf{v}_h)_{\mathcal{T}_h} + \mathcal{C}_h(\mathbf{u}_h; \mathbf{u}_h, \mathbf{v}_h) = 0, \quad \forall \mathbf{v}_h \in \widetilde{\mathbf{V}}_{h,0}^{k,-1}.$$

A corresponding implementation of an explicit fully discrete scheme in the spirit of subsection 2.4 can be obtained easily.

### 3. NAVIER-STOKES EQUATIONS

Now, we consider extending the scheme (6) to the following incompressible Navier-Stokes equations with free-slip boundary conditions:

$$\partial_t \mathbf{u} + (\mathbf{u} \cdot \nabla) \mathbf{u} + \nabla p - \nu \Delta \mathbf{u} = \mathbf{f}, \quad \text{in } \Omega, \tag{16a}$$

$$\nabla \cdot \mathbf{u} = 0, \quad \text{in } \Omega, \tag{16b}$$

$$\mathbf{u} \cdot \mathbf{n} = 0, \quad \text{on } \partial\Omega, \tag{16c}$$

$$\nu((\nabla \mathbf{u}) \mathbf{n}) \times \mathbf{n} = 0, \quad \text{on } \partial\Omega, \tag{16d}$$

with a divergence-free initial condition

$$\mathbf{u}(x, 0) = \mathbf{u}_0(x) \quad \forall x \in \Omega.$$

Here  $\nu = 1/\text{Re}$  is the viscosity. Again, we point out that other boundary conditions such as inflow/outflow/wall boundary conditions can be easily applied.

We discretize the viscous term using symmetric interior penalty DG method [2]. The semi-discrete scheme reads as follows: find  $\mathbf{u}_h(t) \in \mathbf{V}_h^{k,-1}$  such that

$$(\partial_t \mathbf{u}_h, \mathbf{v}_h)_{\mathcal{T}_h} + \mathcal{C}_h(\mathbf{u}_h; \mathbf{u}_h, \mathbf{v}_h) + \mathcal{B}_h(\mathbf{u}_h, \mathbf{v}_h) = 0, \quad \forall \mathbf{v}_h \in \mathbf{V}_h^{k,-1}, \tag{17}$$



where the advective trilinear form  $\mathcal{C}_h$  is given by (7), and the viscous bilinear form  $\mathcal{B}_h$  is given below

$$\begin{aligned} \mathcal{B}_h(\mathbf{u}_h, \mathbf{v}_h) := & \sum_{T \in \mathcal{T}_h} \int_T \nu \nabla \mathbf{u} : \nabla \mathbf{v} \, dx \\ & - \sum_{F \in \mathcal{F}_h^i} \int_F \nu \llbracket \nabla \mathbf{u}_h \rrbracket \llbracket \mathbf{v}_h \otimes \mathbf{n} \rrbracket \, ds \\ & - \sum_{F \in \mathcal{F}_h^i} \int_F \nu \llbracket \nabla \mathbf{v}_h \rrbracket \llbracket \mathbf{u}_h \otimes \mathbf{n} \rrbracket \, ds \\ & + \sum_{F \in \mathcal{F}_h^i} \int_F \nu \frac{\alpha k^2}{h} \llbracket \mathbf{u}_h \otimes \mathbf{n} \rrbracket \llbracket \mathbf{v}_h \otimes \mathbf{n} \rrbracket \, ds, \end{aligned} \quad (18)$$

with  $\alpha > 0$  a sufficiently large stabilization constant.

For a fully discrete scheme, we use the same explicit stepping as the inviscid case. As mentioned in the introduction, our explicit method shall be applied to high Reynolds number flows such that the mesh Reynolds number  $Re_h$  defined in (1) is not too small to avoid severe time stepping restrictions.

#### 4. NUMERICAL RESULTS

In this section, we present several numerical results in two dimensions. The numerical results are performed using the NGSolve software [27]. The first four tests are performed on triangular meshes, where the last one on a rectangular mesh (with the obvious modification of the divergence-conforming space from BDM [6] to RT [24]). For the viscous operator (18), we take the stabilization parameter  $\alpha$  to be 2. We use the TVD-RK3 time stepping (8) with sufficiently small time step size for all the tests, except for **Example 1b** where the classical fourth order Runge-Kutta method is also used to check the temporal accuracy. We use a pre-factored sparse-Cholesky factorization for the hybrid-mixed Poisson solver that is needed in each time step.

**Example 1a: Spatial accuracy test.** This example is used to check the spatial accuracy of our schemes, both for the Euler equations (3) and for the Navier-Stokes equations (16) with  $Re = 100$ . Following [21], we take the domain to be  $[0, 2\pi] \times [0, 2\pi]$  and use a periodic boundary condition. The initial condition and source term are chosen such that the exact solution is

$$u_1 = -\cos(x) \sin(y) \exp(-2t/Re), u_2 = \sin(x) \cos(y) \exp(-2t/Re).$$

The  $L^2$ -errors in velocity at  $t = 1$  on unstructured triangular meshes are shown in Table 1. It is clear to observe optimal  $(k + 1)$ -th order of convergence for both cases.

**Example 1b: Temporal accuracy test.** This example is used to check the temporal accuracy of our schemes. We consider the Navier-Stokes equation (16) with  $\nu = 1/4000$  on a periodic domain  $\Omega = [0, 2\pi] \times [0, 2\pi]$  with the following exact solution

$$u_1 = \sin(6\pi t) \sin(y), u_2 = \sin(6\pi t) \sin(2x).$$

We use a  $P^6$  scheme (17) on a fixed triangular mesh with mesh size  $h = 2\pi/32$  to keep the spatial error small. For the time discretization, we consider either the

TABLE 1. **Example 1a:** History of convergence of the  $L^2$ -velocity errors.

$k$	$h$	Euler		Navier-Stokes	
		error	eoc	error	eoc
1	0.7854	2.339e-01	–	2.234e-01	–
	0.3927	5.638e-02	2.05	5.195e-02	2.10
	0.1963	1.446e-02	1.96	1.250e-02	2.06
	0.0982	3.616e-03	2.00	2.882e-03	2.12
2	0.7854	2.411e-02	–	2.193e-02	–
	0.3927	2.491e-03	3.27	2.142e-03	3.36
	0.1963	2.968e-04	3.07	2.488e-04	3.11
	0.0982	3.514e-05	3.08	2.792e-05	3.16
3	0.7854	1.495e-03	–	1.338e-03	–
	0.3927	7.883e-05	4.25	6.876e-05	4.28
	0.1963	4.969e-06	3.99	4.392e-06	3.97
	0.0982	2.907e-07	4.10	2.701e-07	4.02

TVD-RK3 scheme (8), or the classical four-stage, fourth order Runge-Kutta (RK4) scheme. The  $L^2$ -errors in velocity at  $t = 0.1$  with different time step size are shown in Table 2. It is clear to observe third order of convergence for TVD-RK3, and fourth order of convergence for RK4.

TABLE 2. **Example 1b:** History of convergence of the  $L^2$ -velocity errors.

$\Delta t$	TVD-RK3		RK4	
	error	eoc	error	eoc
0.1/4	3.301e-04	–	1.688e-04	–
0.1/8	3.654e-05	3.18	1.098e-05	3.94
0.1/16	4.459e-06	3.03	6.998e-07	3.97
0.1/32	5.580e-07	3.00	4.414e-08	3.99

**Example 2: Double shear layer problem.** We consider the double shear layer problem used in [5, 21]. The Euler equation (3) on the domain  $[0, 2\pi] \times [0, 2\pi]$  with a periodic boundary condition and an initial condition:

$$u_1(x, y, 0) = \begin{cases} \tanh((y - \pi/2)/\rho) & y \leq \pi \\ \tanh((3\pi/2 - y)/\rho) & y > \pi \end{cases}, \quad (19)$$

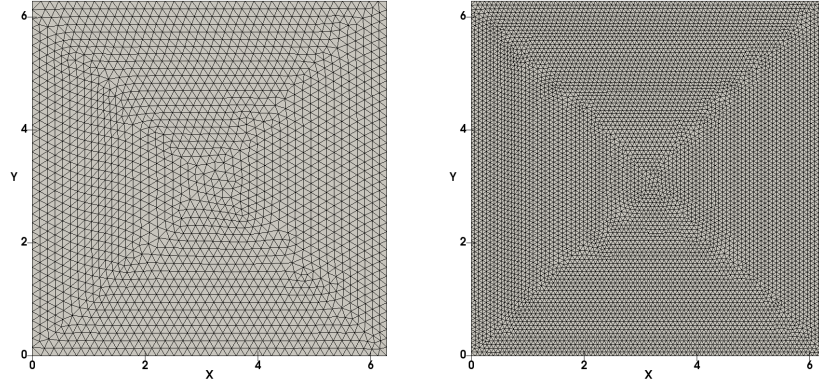
$$u_2(x, y, 0) = \delta \sin(x), \quad (20)$$

with  $\rho = \pi/15$  and  $\delta = 0.05$ .

We use  $P^3$  approximation on fixed uniform unstructured triangular meshes with mesh size  $2\pi/40$  and  $2\pi/80$ , see Fig. 1, and run the simulation up to time  $t = 8$ . We plot the time history of total energy (square of the  $L^2$ -norm of velocity  $\mathbf{u}_h$ ) and total enstrophy (square of  $L^2$ -norm of vorticity  $\omega_h := \nabla_h \times \mathbf{u}_h$ ) in Fig. 2, as well as contours of the vorticity at  $t = 6$  and  $t = 8$  in Fig. 3 to show the resolution.

We can see from Fig. 2 that the energy is monotonically decreasing, with a very small dissipation error. The dissipated energy at time  $t = 8$  for the scheme on the coarse mesh is about  $2 \times 10^{-3}$ , while that on the fine mesh is about  $2 \times 10^{-4}$ . The dissipation in enstrophy is more severe, where we also observe a fluctuation, probably due to the fact that vorticity  $\omega_h$  is a derived variable from the velocity computation. Our results are qualitatively similar to those obtained in [21] that use a vorticity-stream function formulation, with roughly a similar computational cost.

FIGURE 1. Example 2: the computational mesh. Left: coarse mesh. Right: fine mesh.



**Example 3: Kelvin-Helmholtz instability problem.** We consider the Kelvin-Helmholtz instability problem, the set-up is taken from [28]. The Navier-Stokes equations (16) with Reynolds number  $\text{Re} = 10000$  on the domain  $[0, 1] \times [0, 1]$  with a periodic boundary condition on the  $x$ -direction, and the free-slip boundary condition  $\mathbf{u} \cdot \mathbf{n} = 0$ ,  $\nu((\nabla \mathbf{u})\mathbf{n}) \times \mathbf{n} = 0$  at  $y = 0$  and  $y = 1$ . The initial conditions are taken to be

$$\begin{aligned} u_1(x, y, 0) &= u_\infty \tanh((2y - 1)/\delta_0) + c_n \partial_y \psi(x, y), \\ u_2(x, y, 0) &= -c_n \partial_x \psi(x, y), \end{aligned}$$

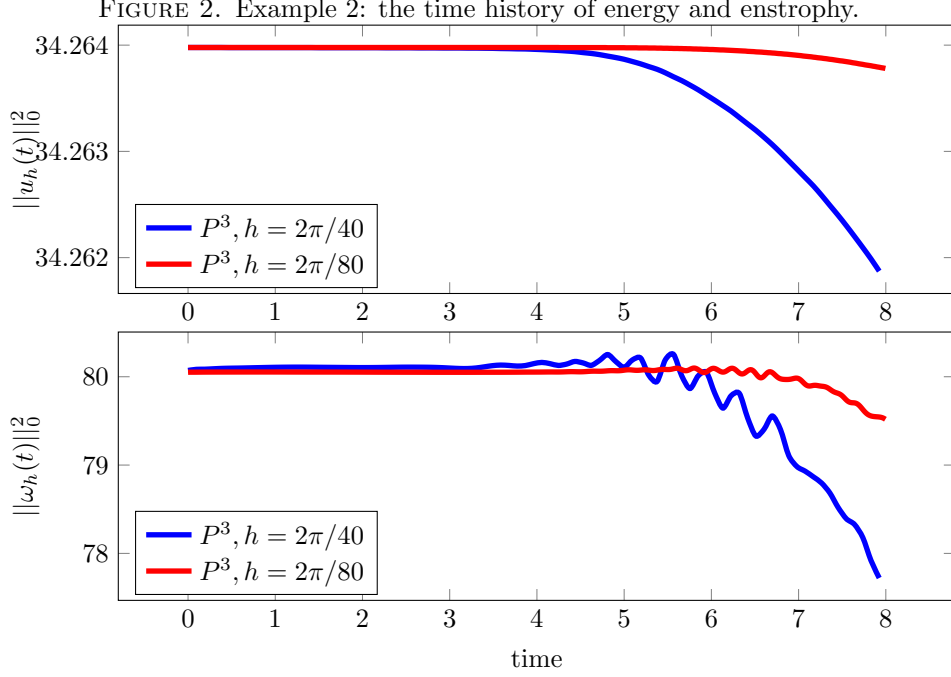
with corresponding stream function

$$\psi(x, y) = u_\infty \exp(-(y - .5)^2/\delta_0^2) [\cos(5\pi x) + \cos(20\pi x)].$$

Here,  $\delta_0 = 1/28$  denotes the vorticity thickness,  $u_\infty = 1$  is a reference velocity and  $c_n = 10^{-3}$  is a scaling/noise factor. The scaled time  $\bar{t} = \delta_0/u_\infty t$  is introduced.

We use a  $P^4$  scheme (17) with TVD-RK3 time stepping on an unstructured triangular mesh with mesh size  $h = 1/80$ . The time step size is taken to be  $\Delta t = \delta_0 \times 10^{-2}$ . We run the simulation till time  $\bar{t} = 400$  (a total of 40,000 time steps). The computation is performed on a desktop machine with 2 dual core CPUs, and about 20 hours wall clock time is used for the overall simulation.

The time evolution of vortices are shown in Fig. 4 up to time  $\bar{t} = 200$ . In the first row, the transition from the initial condition to the four primary vortices is shown. The four vortices are unstable in the sense that they have the tendency to merge. This is a well-known property of two-dimensional flows for which energy



is transferred from the small to the large scales. We observe the second merging process is completed at around  $\bar{t} = 56$ , while the last merging process completed around  $\bar{t} = 160$ , and at time  $\bar{t} = 200$  a single vortex is left. Comparing with the reference data [28], computed using an IMEX SBDF2,  $P^8$  divergence-conforming HDG scheme [28] on a  $256 \times 256$  uniform square mesh with time step size  $\Delta t = \delta_0 \times 10^{-3} \approx 3.6 \times 10^{-5}$ , we observe quite a good agreement of the vorticity dynamics up to time  $\bar{t} = 56$  where the second merging process is completed. However, the numerical results in [28] show that the last merging appears in a much later time, at around  $\bar{t} = 250$ . The numerical dissipation in our simulation triggered the last vortex merging in a much earlier time, since we use a lower order method on a coarser mesh compared with [28]. We notice that a numerical simulation at the scale of [28] is out of reach for our desktop-based simulation.

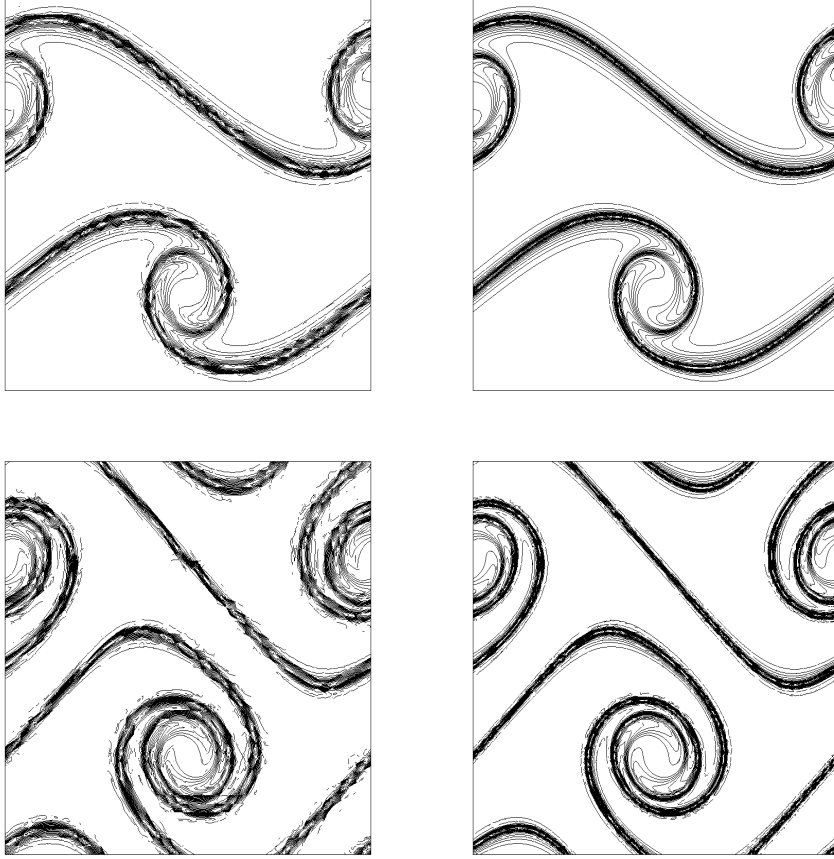
In Fig. 5, we plot the evolution of kinetic energy and enstrophy of our simulation, together with the reference data provided in [28]. A good agreement of the kinetic energy can be clearly seen, while the enstrophy agrees pretty well till time  $\bar{t} = 150$ , where the last vortex merging took place for our simulation, while that happens at a much later time  $\bar{t} = 250$  for the scheme used in [28].

**Example 4: flow around a cylinder.** We consider the 2D-2 benchmark problem proposed in [26] where a laminar flow around a cylinder is considered. The domain is a rectangular channel without an almost vertically centered circular obstacle, c.f. Fig. 6,

$$\Omega := [0, 2.2] \times [0, 0.41] \setminus \{ \|(x, y) - (0.2, 0.2)\|_2 \leq 0.05 \}.$$

The boundary is decomposed into  $\Gamma_{in} := \{x = 0\}$ , the inflow boundary,  $\Gamma_{out} := \{x = 2.2\}$ , the outflow boundary, and  $\Gamma_{wall} := \partial\Omega \setminus (\Gamma_{in} \cup \Gamma_{out})$ , the wall boundary.

FIGURE 3. Example 2: Contour of vorticity. 30 equally spaced contour lines between  $-4.9$  and  $4.9$ . Left: results on the coarse mesh; right: results on the fine mesh. Top:  $t = 6$ ; bottom:  $t = 8$ .  $P^3$  approximation.



On  $\Gamma_{out}$  we prescribe natural boundary conditions  $(-\nu \nabla \mathbf{u} + pI)\mathbf{n} = 0$ , on  $\Gamma_{wall}$  homogeneous Dirichlet boundary conditions for the velocity (no-slip) and on  $\Gamma_{in}$  the inflow Dirichlet boundary conditions

$$\mathbf{u}(0, y, t) = 6\bar{u}y(0.41 - y)/0.41^2 \cdot (1, 0),$$

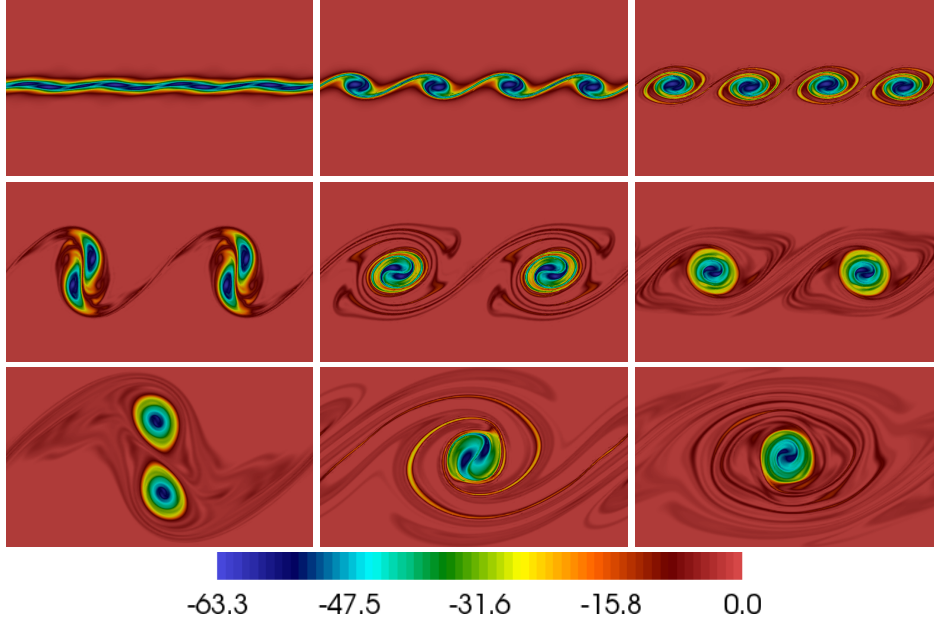
with  $\bar{u} = 1$  the average inflow velocity. The viscosity is taken to be  $\nu = 10^{-3}$ , hence Reynolds number  $\text{Re} = \bar{u}D/\nu = 100$ , where  $D = 0.1$  is the disc diameter.

The quantities of interest in this example are the (maximal and minimal) drag and lift forces  $c_D$ ,  $c_L$  that act on the disc. These are defined as

$$[c_D, c_L] = \frac{1}{\bar{u}^2 r} \int_{\Gamma_o} (\nu \nabla \mathbf{u} - pI)\mathbf{n} ds,$$

where  $r = 0.05$  is the radius of the obstacle, and  $\Gamma_o$  denotes the surface of the obstacle.

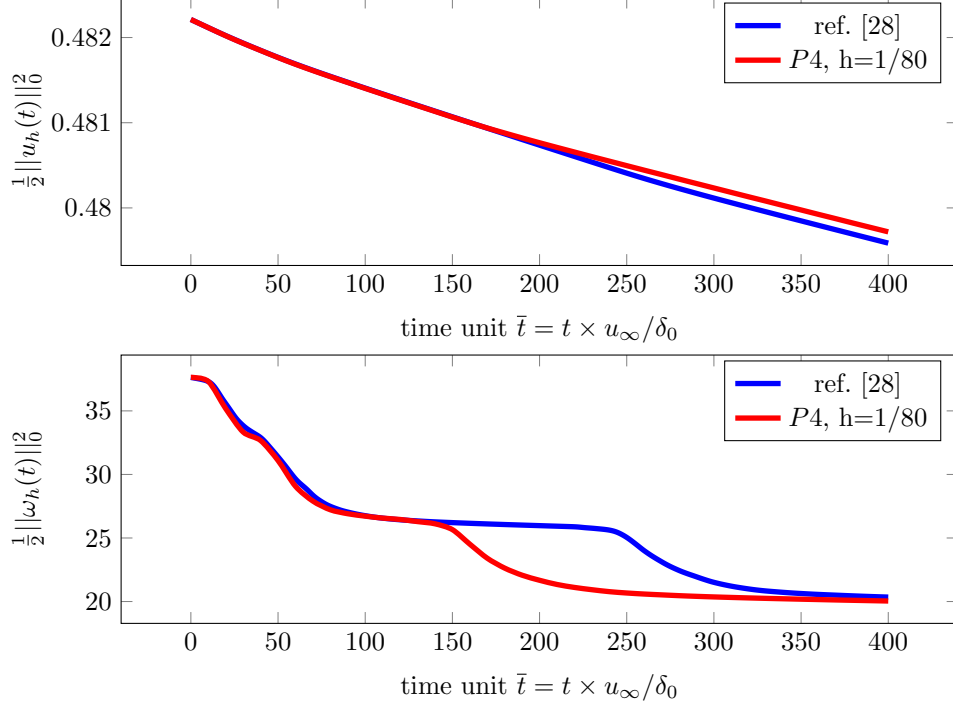
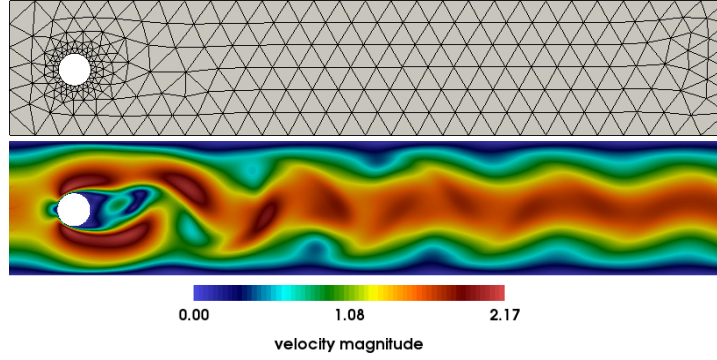
FIGURE 4. Example 3: Contour of vorticity  $\omega_h := \nabla_h \times \mathbf{u}_h$  at (from left to right and top to bottom) time  $\bar{t} = \{5, 10, 17, 34, 56, 80, 120, 160, 200\}$ .



We use a (curved) unstructured triangular grid around the disk. In Fig. 6 the geometry, the mesh and a typical solution is depicted. The final time of the simulation is taken to be  $t = 8$ . The mesh consists of 488 triangular elements with mesh size  $h \approx 0.013$  around the circle (24 uniformly spaced nodes on the circle), and  $h \approx 0.08$  away from the circle. We run the simulation on this mesh using polynomial degree from 2 to 4. The maximal/minimal drag and lift coefficients are listed in Table 3, where the local dofs refer to those for velocity and pressure, while the global dofs refer to those for the Lagrange multiplier on the mesh skeleton. As a reference, we also show the results obtained by FEATFLOW [12] using a  $Q^2/P^{1,\text{disc}}$  quadrilateral element. Clearly we observe a rapid convergence as the polynomial degree increases. Compared with the (low-order) results from the literature [12], the same accuracy is achieved with a lot less degrees of freedom. Similar observation was also found for the divergence-conforming IMEX-HDG scheme [20].

**Example 5: lid driven cavity at a high Reynolds number.** In our last example, we consider a lid driven cavity flow problem [13] at a high Reynolds number  $\text{Re} = 10,000$ . The domain is a unit square  $\Omega = [0, 1] \times [0, 1]$ , the velocity boundary condition is used on the boundary with  $(u_1, u_2) = (1, 0)$  on the top boundary  $y = 1$ , and  $(u_1, u_2) = (0, 0)$  on the other boundaries. We use a steady-state Solver solver to generate the initial condition. For this problem, the solution eventually reaches a steady state. However, for such high Reynolds number flow, the numerical solution tends to oscillate around the steady-state without settling down on coarse meshes, see e.g. the discussion in [11].

FIGURE 5. Example 3: the time history of energy and enstrophy.

FIGURE 6. Example 4: Sketch of the mesh and the solution using the  $P^4$  scheme (color corresponding to velocity magnitude  $\|\mathbf{u}\|_2$ ).

We consider a uniform  $32 \times 32$  rectangular mesh using the divergence-free RT  $Q^4$  velocity space. Since temporal accuracy is not of concern for this problem. We use the cheaper forward Euler time stepping (9). The time step size is taken to be  $\Delta t = 10^{-3}$ . Final time of simulation is  $t = 400$ . Hence, a total of 400,000 time steps is used. For this problem, we have local dofs 37,888(local velocity and pressure) and global dofs 10,560(Lagrange multiplier). The overall wall computational time is about 10 hours.

TABLE 3. Example 4: Maximal/minimal values of lift and drag coefficients: results for different polynomial degree.

	#dof local	#dof global	max $c_D$	min $c_D$	max $c_L$	min $c_L$
k=2	5 368	2 316	3.132939	3.074858	0.935284	-0.884771
k=3	7 808	3 088	3.229686	3.170424	0.969323	-0.965982
k=4	10 736	3 860	3.226865	3.163545	0.986497	-1.018691
ref.	-	167 232	3.22662	3.16351	0.98620	-1.02093
[12]	-	667 264	3.22711	3.16426	0.98658	-1.02129

In Fig. 7 and Fig. 8, we plot the time evolution of the streamlines and vorticity contours. We numerically observe that starting around time  $t = 80$ , the solution oscillates around the steady-state solution but never reaches the steady state. The  $L^2$ -norm of the velocity difference at two consecutive time levels hangs at around  $5 \times 10^{-5}$  and never drops down. This phenomenon is probably due to the low mesh resolution ( $32 \times 32$  in our case). In particular, for second-order methods, a mesh larger than  $256 \times 256$  shall be used to reach a steady-state for high Reynolds number flow ( $Re > 10,000$ ); see [11]. However, the main features of the small structure around the top, left and right corners can be clearly seen in Fig. 7 and Fig. 8 starting at time  $t = 80$ . Finally, in Fig. 9, we plot the  $x$ -component of velocity field along the horizontal central line  $x = 0.5$ , and the  $y$ -component of velocity field along the vertical central line  $y = 0.5$  at time  $t = 160, 200, 400$ , along with the reference data provided in [13]. A good match with the reference data is observed.

## 5. CONCLUSION

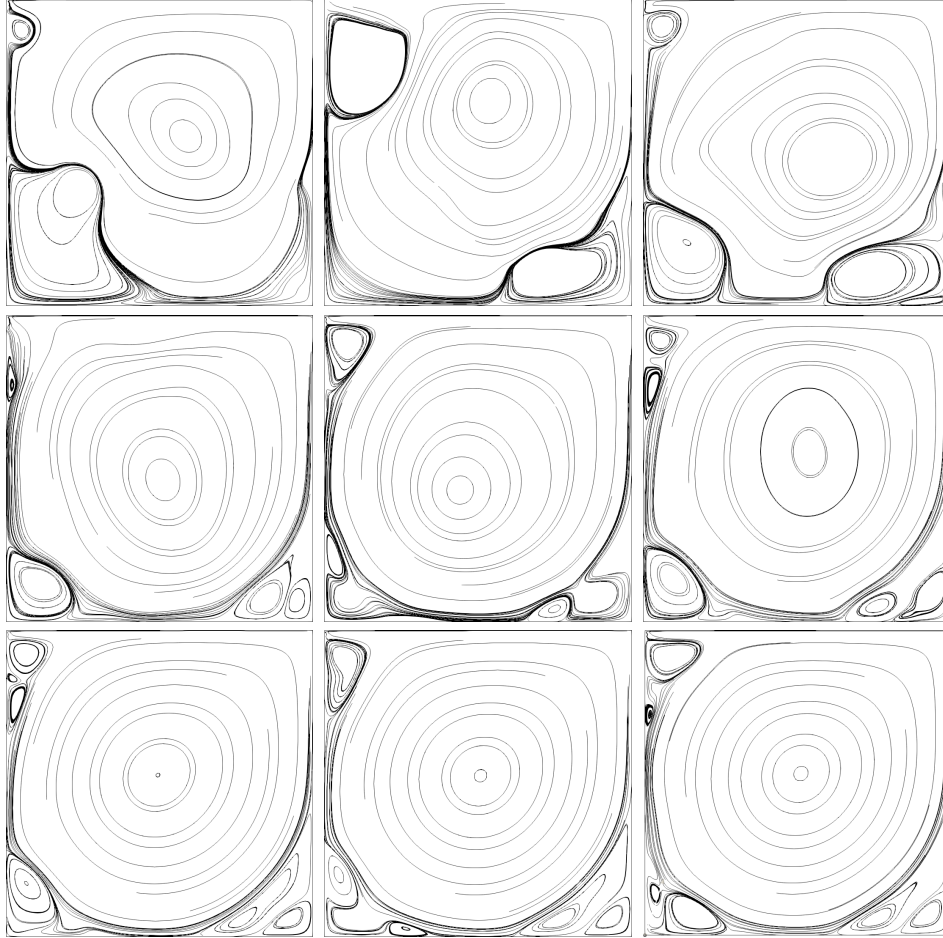
We presented an explicit divergence-free DG method for incompressible flows. The key ingredient for the efficient implementation is the identification of the equivalence of the mass matrix inversion of the divergence-free finite element space and a hybrid-mixed Poisson solver. The scheme is especially suitable for unsteady inviscid flow or viscous flow at a high Reynolds number flow.

## REFERENCES

- [1] D. N. ARNOLD AND F. BREZZI, *Mixed and nonconforming finite element methods: implementation, postprocessing and error estimates*, RAIRO Modél. Math. Anal. Numér., 19 (1985), pp. 7–32.
- [2] D. N. ARNOLD, F. BREZZI, B. COCKBURN, AND L. D. MARINI, *Unified analysis of discontinuous Galerkin methods for elliptic problems*, SIAM J. Numer. Anal., 39 (2001/02), pp. 1749–1779.
- [3] D. N. ARNOLD, R. S. FALK, AND R. WINTHER, *Finite element exterior calculus, homological techniques, and applications*, Acta Numer., 15 (2006), pp. 1–155.
- [4] U. M. ASCHER, S. J. RUUTH, AND R. J. SPITERI, *Implicit-explicit Runge-Kutta methods for time-dependent partial differential equations*, Appl. Numer. Math., 25 (1997), pp. 151–167. Special issue on time integration (Amsterdam, 1996).
- [5] J. B. BELL, P. COLELLA, AND H. M. GLAZ, *A second-order projection method for viscous, incompressible flow*, in AIAA 8th Computational Fluid Dynamics Conference (Honolulu, HI, 1987), AIAA, Washington, DC, 1987, pp. 789–794.

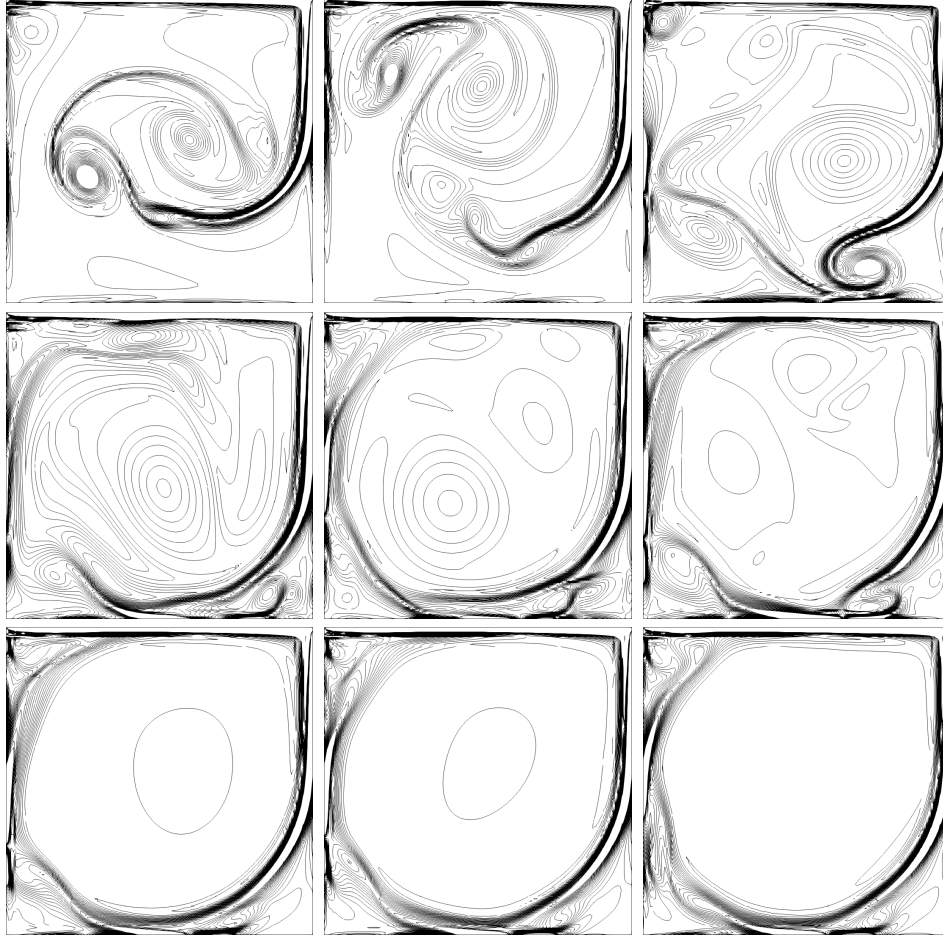


FIGURE 7. Example 5: Streamline plots at (from left to right and top to bottom) time  $t = \{2, 4, 10, 20, 40, 80, 160, 200, 400\}$ .



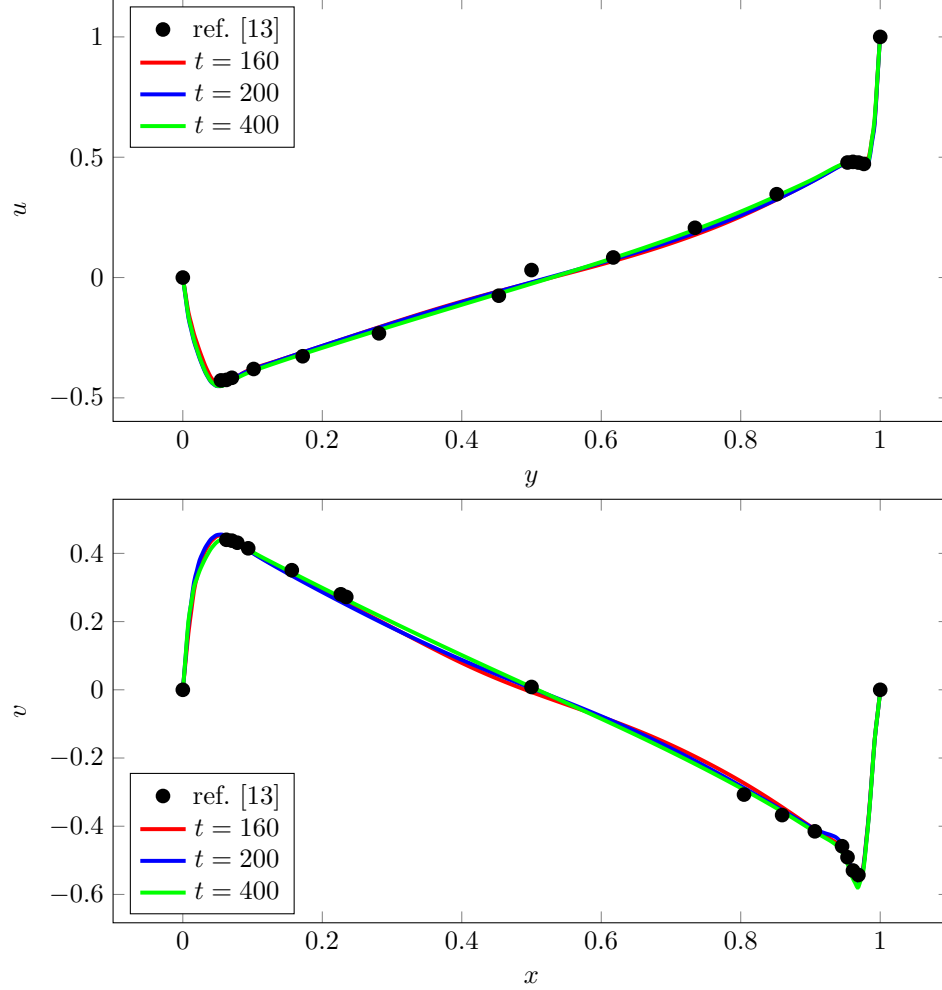
- [6] F. BREZZI, J. DOUGLAS, JR., AND L. D. MARINI, *Two families of mixed finite elements for second order elliptic problems*, Numer. Math., 47 (1985), pp. 217–235.
- [7] M. P. CALVO, J. DE FRUTOS, AND J. NOVO, *Linearly implicit Runge-Kutta methods for advection-reaction-diffusion equations*, Appl. Numer. Math., 37 (2001), pp. 535–549.
- [8] B. COCKBURN, G. KANSCHAT, AND D. SCHÖTZAU, *A note on discontinuous Galerkin divergence-free solutions of the Navier-Stokes equations*, J. Sci. Comput., 31 (2007), pp. 61–73.
- [9] W. E AND J.-G. LIU, *Vorticity boundary condition and related issues for finite difference schemes*, J. Comput. Phys., 124 (1996), pp. 368–382.
- [10] ———, *Finite difference methods for 3D viscous incompressible flows in the vorticity-vector potential formulation on nonstaggered grids*, J. Comput. Phys., 138 (1997), pp. 57–82.
- [11] E. ERTURK, *Discussions on driven cavity flow*, Internat. J. Numer. Methods Fluids, 60 (2009), pp. 275–294.
- [12] FEATFLOW, *Finite element software for the incompressible navier-stokes equations*, [www.featflow.de](http://www.featflow.de).
- [13] U. GHIA, N. GHIA, AND C. T. SHIN, *High-Re Solutions for Incompressible Flow Using the Navier-Stokes Equations and a Multigrid Method*, J. Comput. Phys., 48 (1982), pp. 387–411.

FIGURE 8. Example 5: Contour of vorticity at (from left to right and top to bottom) time  $t = \{2, 4, 10, 20, 40, 80, 160, 200, 400\}$ . 30 equally spaced contours between  $-1$  to  $1$ .



- [14] R. GLOWINSKI, *Finite element methods for incompressible viscous flow*, in Handbook of numerical analysis, Vol. IX, Handb. Numer. Anal., IX, North-Holland, Amsterdam, 2003, pp. 3–1176.
- [15] J. L. GUERMOND, P. MINEV, AND J. SHEN, *An overview of projection methods for incompressible flows*, Comput. Methods Appl. Mech. Engrg., 195 (2006), pp. 6011–6045.
- [16] J. GUZMÁN, C.-W. SHU, AND F. A. SEQUEIRA, *H(div) conforming and DG methods for incompressible Euler’s equations*, IMA J. Numer. Anal., 37 (2017), pp. 1733–1771.
- [17] V. JOHN, A. LINKE, C. MERDON, M. NEILAN, AND L. G. REBHOLZ, *On the divergence constraint in mixed finite element methods for incompressible flows*, SIAM Rev., 59 (2017), pp. 492–544.
- [18] C. A. KENNEDY AND M. H. CARPENTER, *Additive Runge-Kutta schemes for convection-diffusion-reaction equations*, Appl. Numer. Math., 44 (2003), pp. 139–181.
- [19] C. LEHRENFELD, *Hybrid Discontinuous Galerkin methods for solving incompressible flow problems*, 2010. Diploma Thesis, MathCCES/IGPM, RWTH Aachen.

FIGURE 9. Example 5: velocity along cut lines. Top:  $x$ -component velocity on horizontal central line  $x = 0.5$ ; bottom:  $y$ -component velocity on vertical central line  $y = 0.5$ .



- [20] C. LEHRENFELD AND J. SCHÖBERL, *High order exactly divergence-free hybrid discontinuous galerkin methods for unsteady incompressible flows*, Computer Methods in Applied Mechanics and Engineering, 307 (2016), pp. 339–361.
- [21] J.-G. LIU AND C.-W. SHU, *A high-order discontinuous Galerkin method for 2D incompressible flows*, J. Comput. Phys., 160 (2000), pp. 577–596.
- [22] Y. MADAY, A. T. PATERA, AND E. M. RØNQUIST, *An operator-integration-factor splitting method for time-dependent problems: application to incompressible fluid flow*, J. Sci. Comput., 5 (1990), pp. 263–292.
- [23] A. MONTLAUR, S. FERNANDEZ-MENDEZ, J. PERAIRE, AND A. HUERTA, *Discontinuous Galerkin methods for the Navier-Stokes equations using solenoidal approximations*, Internat. J. Numer. Methods Fluids, 64 (2010), pp. 549–564.
- [24] P. A. RAVIART AND J. M. THOMAS, *A mixed finite element method for second order elliptic problems*, in Mathematical Aspects of Finite Element Method, Lecture Notes in Math. 606, I. Galligani and E. Magenes, eds., Springer-Verlag, New York, 1977, pp. 292–315.

- [25] S. ZAGLMAYR, *High order finite element methods for electromagnetic field computation*, 2006. PhD thesis, Johannes Kepler Universit ät Linz, Linz.
- [26] M. SCHÄFER, S. TUREK, F. DURST, K. E., AND R. R., *Benchmark computations of laminar flow around a cylinder*, Flow simulation with high-performance computers II 1996; :547566.
- [27] J. SCHÖBERL, *C++11 Implementation of Finite Elements in NGSolve*, 2014. ASC Report 30/2014, Institute for Analysis and Scientific Computing, Vienna University of Technology.
- [28] P. W. SCHROEDER, V. JOHN, P. L. LEDERER, C. LEHRENFELD, G. LUBE, AND J. SCHÖBERL, *On reference solutions and the sensitivity of the 2d Kelvin–Helmholtz instability problem*, arXiv preprint arXiv:1803.06893, (2018).
- [29] C.-W. SHU AND S. OSHER, *Efficient implementation of essentially nonoscillatory shock-capturing schemes*, J. Comput. Phys., 77 (1988), pp. 439–471.

DIVISION OF APPLIED MATHEMATICS, BROWN UNIVERSITY, 182 GEORGE ST, PROVIDENCE RI 02912, USA.

*E-mail address*: Guosheng\_Fu@brown.edu